

# Technical Report

TR-2012-011

**Iterative Wavefront Reconstruction for Astronomical Imaging**

by

Q. Chu, S. Jefferies, J. G. Nagy

**MATHEMATICS AND COMPUTER SCIENCE**

**EMORY UNIVERSITY**

# ITERATIVE WAVEFRONT RECONSTRUCTION FOR ASTRONOMICAL IMAGING

QING CHU\*, STUART JEFFERIES†, AND JAMES G. NAGY‡

**Abstract.** Obtaining high resolution images of space objects from ground based telescopes is challenging, and often requires computational post processing methods to remove blur caused by atmospheric turbulence. In order for an image deblurring (deconvolution) algorithm to be effective, it is important to have a good approximation of the blurring operator. In space imaging, the blurring operator is defined in terms of the wavefront of light, and how it is distorted as it propagates through the atmosphere. In this paper we describe an approach to reconstruct the wavefront. Accuracy is obtained by exploiting, and fusing, information from multiple measurements. Mathematically, this process involves solving a sparse, large-scale linear least squares problem. The least squares problem is efficiently solved using a conjugate gradient type method, such as LSQR.

**Key words.** image deblurring, multiframe deconvolution, frozen flow hypothesis, least squares, astronomical imaging, conjugate gradient method, LSQR

**AMS Subject Classifications:** 65F20, 65F30

**1. Introduction.** In many imaging situations, such as when ground based telescopes are used to observe objects in space, the observed image is degraded by blurring and noise. Although the blurring can be partially removed through sophisticated (and expensive) imaging devices, such as adaptive optics telescopes, computational post-processing techniques are also often needed to further improve the resolution of the image.

This computational postprocessing, which is referred to as deblurring, restoration, or deconvolution [15, 24], requires solving an ill-posed inverse problem

$$g(x, y) = \int_{\mathcal{R}^2} k(x, y; \xi, \eta) f(\xi, \eta) d\xi d\eta + e(x, y), \quad (1.1)$$

where  $f$  is the true object,  $g$  is the observed image, and  $e$  is additive noise. The kernel function  $k$  models the blurring operation, and is called the *point spread function* (PSF). In many applications the kernel satisfies  $k(x, y; \xi, \eta) = k(x - \xi, y - \eta)$ , and the blur is said to be spatially invariant. In this case, the integration in equation (1.1) is a *convolution* operation.

The digital image deblurring problem is obtained from equation (1.1) by discretizing the functions and approximating integration with a quadrature rule:

$$\mathbf{g} = \mathbf{K}\mathbf{f} + \mathbf{e}. \quad (1.2)$$

If the images are assumed to have  $m \times n$  pixels, then  $\mathbf{K} \in \mathcal{R}^{mn \times mn}$  and  $\mathbf{g}, \mathbf{f}, \mathbf{e} \in \mathcal{R}^{mn}$ . The matrix  $\mathbf{K}$  is typically very ill-conditioned; more severe blurring usually corresponds with a more ill-conditioned  $\mathbf{K}$ . In the case  $k(x, y; \xi, \eta) = k(x - \xi, y - \eta)$ ,  $\mathbf{K}$  can involve (depending on the imposed boundary conditions) circulant, Toeplitz, and Hankel structures [13].

---

\*Department of Mathematics and Computer Science, Emory University. Email: qchu@mathcs.emory.edu.

†Institut for Astronomy, University of Hawaii. Email: stuartj@ifa.hawaii.edu. Research supported in part by AFOSR under grant FA9550-09-1-0216.

‡Department of Mathematics and Computer Science, Emory University. Email: nagy@mathcs.emory.edu. Research supported in part by the AFOSR under grant FA9550-09-1-0487.

A substantial amount of research has been done to develop effective methods to compute approximate solutions of equation (1.2); see, for example [5, 11, 12, 24]. Much of this is well known to the numerical linear algebra and scientific computing research communities. However, most research on digital image deblurring algorithms assume that the matrix  $\mathbf{K}$  is known, but in fact in most realistic applications  $\mathbf{K}$  must be approximated from additional measured data. The quality of the reconstructed image can depend strongly on the quality of this approximation.

In this paper we highlight one such application that arises when imaging objects in space from ground based telescopes, where the blurring is caused by atmospheric turbulence. In this application the PSF is defined in terms of the wavefront of light incoming to the telescope; a planer wavefront corresponds to excellent seeing conditions (little blur in the image), while a highly oscillatory wavefront corresponds to poor seeing conditions. A theoretical model of the PSF is given in Section 2. In Section 3 we provide a brief review of Tikhonov regularization and fast Fourier transform (FFT) based image deblurring. In Section 4 we describe how a *wavefront sensor* (WFS) on the telescope can be used to reconstruct approximations of the wavefront (and, hence, the PSF and the matrix  $\mathbf{K}$ ). In particular, we describe an approach to improve the resolution capabilities of the WFS using multiple frames of data. Algebraically the scheme requires solving a large scale, sparse least squares problem. Finally, in Section 5 we show examples, from simulated data, of the effectiveness of our methods. Some concluding remarks are given in Section 6.

**2. Blurring Caused by Atmospheric Turbulence.** In this paper we consider imaging objects in space using ground based telescopes, where the PSF  $k$  depends on the wavefront of incoming light at the telescope's mirror; if the wavefront function is known, then  $k$  is known. More specifically,  $k(x, y; \xi, \eta) = k(x - \xi, y - \eta)$ , with

$$k(s, t) = \left| \mathcal{F}^{-1} \left\{ P(s, t) e^{i(1-\omega(s,t))} \right\} \right|^2 = \left| \mathcal{F}^{-1} \left\{ P(s, t) e^{i\phi(s,t)} \right\} \right|^2, \quad (2.1)$$

where  $\omega(s, t)$  is a function that models the shape of the wavefront of incoming light at the telescope,  $i = \sqrt{-1}$ ,  $P(s, t)$  is a characteristic function that models the shape of the telescope aperture (e.g., a circle or an annulus),  $\mathcal{F}^{-1}$  is the 2-dimensional inverse Fourier transform, and  $\phi(s, t) = 1 - \omega(s, t)$  is the phase error, or the deviation from planarity of the wavefront  $\omega$ .

**2.1. Diffraction Limited Imaging.** In the ideal situation, where the atmosphere causes no distortion of the incoming wavefront,  $\omega(s, t) = 1$  and  $\phi(s, t) = 0$ . In this *diffraction limited* case,

$$k_0(s, t) = \left| \mathcal{F}^{-1} \{ P(s, t) \} \right|^2$$

where  $P(s, t)$  is the pupil aperture function. Note that if  $P(s, t) = 1$  for all  $s$  and  $t$ , then  $k_0(s, t)$  is a delta function, and (except for noise) there is no distortion in the observed image  $g$ . However, in a realistic situation,  $P(s, t) = 1$  in at most a finite region (e.g., within a circle or annulus defined by the telescope aperture), and thus it is impossible to obtain a perfect image. The best result we can hope to obtain is the noise free, diffraction limited image

$$f_0(x, y) = \int_{\mathcal{R}^2} k_0(x - \xi, y - \eta) f(\xi, \eta) \cdot$$

Fig. 2.1 shows two examples of diffraction limited images.

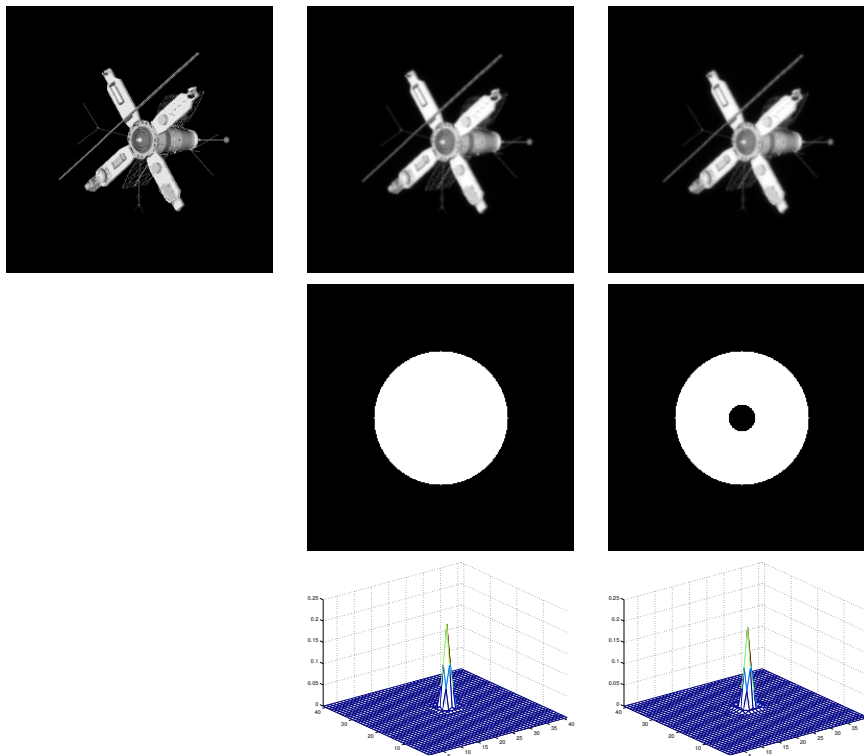


FIG. 2.1. *Examples of diffraction limited images. The top row shows the true object along with the diffraction limited observations with, respectively, a circular and an annulus pupil aperture,  $P(s, t)$ . The middle row displays the pupil apertures used for this example, and the last row shows the corresponding kernels  $k_0(s, t)$ .*

**2.2. Nonplanar Wavefronts.** In a realistic imaging situation, the incoming wavefront will be distorted by atmospheric turbulence. The severity of blurring caused by atmospheric turbulence depends on many factors, including weather, temperature, wavelength, and the diameter of the telescope. For example, viewing objects directly above the telescope site on a clear night will have significantly better seeing conditions than looking during daylight hours at objects close to the horizon. Astronomers often quantify seeing conditions in terms of the ratio  $d/r_0$ , where  $d$  is the diameter of the telescope and  $r_0$  is called the *Fried parameter*, which is related to the wavelength, and provides a statistical description of the level of atmospheric turbulence at a particular site. It is not essential to understand the precise definitions and characteristics of the Fried parameter, except that:

- Good seeing conditions correspond to “small”  $d/r_0$ , such as  $d/r_0 \lesssim 10$ .
- Poor seeing conditions correspond to “large”  $d/r_0$ , such as  $d/r_0 \gtrsim 20$ .

Fig. 2.2 shows examples of wavefronts phases, kernels and blurred images for both good ( $d/r_0 = 5$ ) and poor ( $d/r_0 = 20$ ) seeing conditions. Note that one should interpret the wavefront phase “images” as color encoded contour plots. That is, these are not actually color images, but we display using a false color map so that it is easier to see how they fluctuate. The color bars show that the severity of the fluctuation, or deviation from planarity, is more significant in the case of poor seeing conditions.

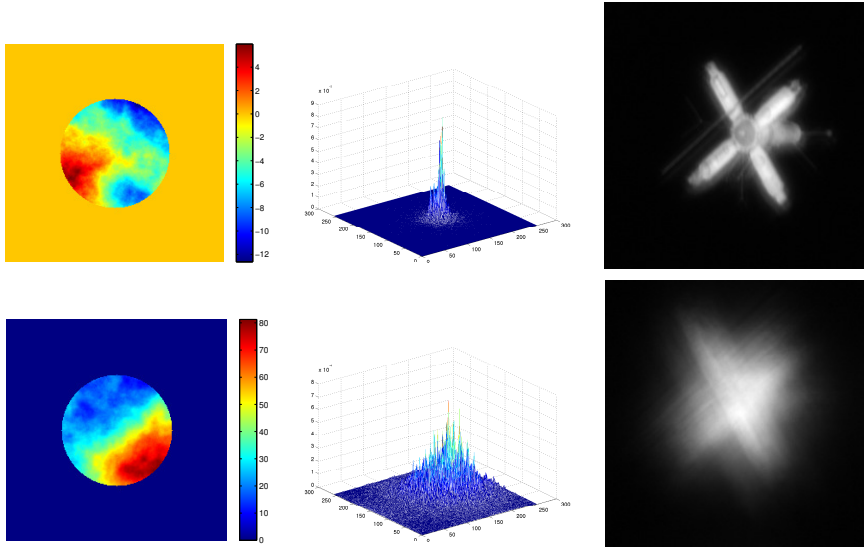


FIG. 2.2. *Examples of good and poor seeing conditions. Each row shows a color contour of a simulated wavefront incident at the telescope, the corresponding blurring kernel and blurred image. The top row illustrates good seeing conditions, with  $d/r_0 = 5$ , and the bottom row illustrates poor seeing conditions with  $d/r_0 = 20$ .*

### 3. FFT Based Image Deblurring.

**3.1. FFT based Tikhonov Regularization.** It is important to emphasize that if  $\mathbf{K}$  is known precisely (or at least to high accuracy) then there are many effective approaches to solve the linear inverse problem (1.2). For example, one of the most well-known schemes is to solve a Tikhonov regularized least squares problem:

$$\min_f \|\mathbf{g} - \mathbf{K}\mathbf{f}\|_2^2 + \alpha^2 \|\mathbf{f}\|_2^2 = \min_f \left\| \begin{bmatrix} \mathbf{g} \\ \mathbf{0} \end{bmatrix} - \begin{bmatrix} \mathbf{K} \\ \alpha \mathbf{I} \end{bmatrix} \mathbf{f} \right\|_2^2.$$

If the PSF is spatially invariant, and we impose periodic boundary conditions to model the image scene outside the field of view, then  $\mathbf{K}$  is a block circulant matrix with circulant blocks. In this case, the spectral decomposition of  $\mathbf{K}$  has the form

$$\mathbf{K} = \mathcal{F}^* \mathbf{\Lambda} \mathcal{F}$$

where  $\mathcal{F}$  is the 2-dimensional unitary discrete Fourier transform matrix,  $\mathcal{F}^* = \mathcal{F}^{-1}$ , and  $\mathbf{\Lambda}$  is a diagonal matrix containing the eigenvalues of  $\mathbf{K}$ . In this case, the solution to the Tikhonov regularized least squares problem can be written as

$$\mathbf{f} = \mathcal{F}^* (|\mathbf{\Lambda}|^2 + \alpha^2 \mathbf{I})^{-1} \bar{\mathbf{\Lambda}} \mathcal{F} \mathbf{g}.$$

Matrix-vector multiplications with  $\mathcal{F}$  and  $\mathcal{F}^*$  can be done very efficiently using, respectively, forward and inverse 2-dimensional fast Fourier transforms (FFT). In addition, the diagonal entries of  $\mathbf{\Lambda}$  can be computed efficiently by computing an FFT of the PSF; for further details, see [24].

Note that there still is the issue of choosing an appropriate  $\alpha$ . There are several approaches; for the numerical tests in this paper we use generalized cross validation

(GCV),

$$\alpha_{\text{gcv}} = \arg \min_{\alpha} \frac{\sum_{i=1}^N (\hat{g}_i / (|\lambda_i|^2 + \alpha^2))^2}{\left( \sum_{i=1}^N 1 / (|\lambda_i|^2 + \alpha^2) \right)^2}.$$

Considering the blurred images in Fig. 2.2, one might think it would be more difficult to reconstruct the image in the poor seeing condition case. However, if the wavefront, and hence the matrix  $\mathbf{K}$ , is exactly known, then a good reconstruction may not be so difficult to obtain. To illustrate this, we added 1% Gaussian white noise to the blurred images in Fig. 2.2, and solved both problems using Tikhonov regularization. In each case, three different regularization parameters were used:  $\alpha_1 = \alpha_{\text{gcv}}$ ,  $\alpha_2 = \sqrt{\alpha_{\text{gcv}}}$  and  $\alpha_3 = \alpha_{\text{gcv}}^2$ . The results are shown in Fig. 3.1. It is possible that better results can be obtained with different regularization parameters, or alternative regularization methods. But the purpose of this example is to illustrate that fairly good reconstructions can be obtained with very simple methods, even if the seeing conditions are poor. The key is that precise knowledge of the matrix  $\mathbf{K}$  must be known.

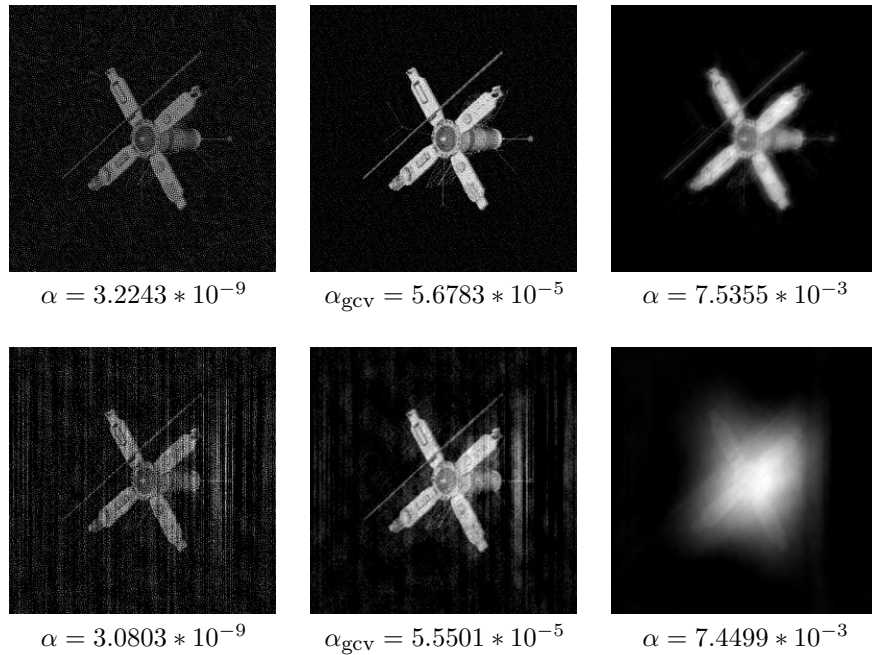


FIG. 3.1. Results of using FFT-based Tikhonov regularization to reconstruct the images shown in Fig. 2.2. The top row shows reconstructions for the case of good seeing conditions, with three different regularization parameters. The bottom row shows similar results for the case of poor seeing conditions.

**3.2. Weighted Least Squares Approach.** As previously mentioned, in most realistic applications the wavefront phase must be estimated from measured data. Therefore the wavefront phase, and hence the matrix  $\mathbf{K}$ , is not precisely known, which

limits the quality of reconstructed images. One approach to improve the quality of the reconstructed image is to collect more data, and solve a *multi-frame* image deconvolution problem. Specifically, several observations of the object are collected, resulting in multiple blurred image frames

$$\mathbf{g}_i = \mathbf{K}_i \mathbf{f} + \mathbf{e}_i, \quad i = 1, 2, \dots, n_{\mathbb{F}}$$

where  $n_{\mathbb{F}}$  is the number of observed image frames. In this case, we can, for example, compute a reconstructed image by solving the overdetermined regularized least squares problem

$$\min_{\mathbf{f}} \left\| \begin{bmatrix} \mathbf{g}_1 \\ \vdots \\ \mathbf{g}_{n_{\mathbb{F}}} \\ \mathbf{0} \end{bmatrix} - \begin{bmatrix} \mathbf{K}_1 \\ \vdots \\ \mathbf{K}_{n_{\mathbb{F}}} \\ \alpha \mathbf{I} \end{bmatrix} \mathbf{f} \right\|_2^2.$$

In the case of spatially invariant blurs with periodic boundary conditions, the solution of this least squares problem can be written as

$$\mathbf{f} = \mathcal{F}^* \left( \sum_{i=1}^{n_{\mathbb{F}}} |\Lambda_i|^2 + \alpha^2 \mathbf{I} \right)^{-1} \left( \sum_{i=1}^{n_{\mathbb{F}}} \bar{\Lambda}_i \mathcal{F} \mathbf{g}_i \right).$$

One problem with using this *ordinary* least squares (OLS) model to restore images is that we assume that the wavefront phase for each frame is estimated with equal accuracy. However, in the next section we describe an approach where we can get better sampling, and hence better estimates, of the wavefront phase for certain frames. In this case, it might be more appropriate to use a *weighted* least squares (WLS) approach [10], to reconstruct the image  $\mathbf{f}$ . The idea is to assign larger weights,  $\omega_i$ , to observation frames with better wavefront estimates. Thus, in the case of spatially invariant blurs with periodic boundary conditions, the WLS solution can be written as

$$\mathbf{f} = \mathcal{F}^* \left( \sum_{i=1}^{n_{\mathbb{F}}} \omega_i |\Lambda_i|^2 + \alpha^2 \mathbf{I} \right)^{-1} \left( \sum_{i=1}^{n_{\mathbb{F}}} \omega_i \bar{\Lambda}_i \mathcal{F} \mathbf{g}_i \right). \quad (3.1)$$

We will use this approach in the numerical experiments in Section 5. But first we discuss the important problem of computing an estimate of the wavefront phase.

**4. Wavefront Reconstruction.** In the previous section we observed that if the matrix  $\mathbf{K}$  is known, then very good results can be computed using fairly simple image deblurring algorithms. The approach one uses to obtain a good approximation of  $\mathbf{K}$  is highly problem dependent. In this paper, we focus specifically on using ground based telescopes to image objects in space. In particular, we consider using telescopes that have a *wavefront sensor* (WFS) that measures gradients of the wavefront. A WFS is standard technology in adaptive optics systems, and many papers have been written about efficiently reconstructing the wavefront from the gradient measurements; see, for example [1, 14, 18]. That is, in addition to observing images, the telescope collects the additional data

$$\begin{bmatrix} \phi_x \\ \phi_y \end{bmatrix} = \begin{bmatrix} \mathbf{W} \mathbf{D}_x \\ \mathbf{W} \mathbf{D}_y \end{bmatrix} \phi + \boldsymbol{\varepsilon}, \quad (4.1)$$

where  $\phi_x$  and  $\phi_y$  are discrete, noisy ( $\varepsilon$  is used to denote noise) measurements of the horizontal and vertical derivatives of  $\phi$ ;  $D_x$  and  $D_y$  are discrete, horizontal and vertical derivative operators. The precise structure of  $D_x$  and  $D_y$  depends on the sensor geometry [6, 14] but they essentially model finite difference approximations.  $W$  is a diagonal matrix containing ones and zeros; one for locations that fall within the pupil aperture, and zero otherwise. Several approaches have been proposed to efficiently solve equation (4.1), including [9, 20]. For the computational experiments reported in this paper, we use the approach described in [2].

**4.1. WFS Limitations.** A difficulty with using equation (4.1) is that the gradient measurements are given on a relatively coarse grid compared to the observed image data. More specifically:

- Generally, to satisfy the Nyquist sampling theorem [17], the ratio of pupil aperture size to number of pixels on the CCD array is 0.5. That is, if the CCD array that collects image data contains  $256 \times 256$  pixels, then the diameter of the pupil aperture is 128 pixels.
- Gradient measurements are taken from a sensor on the mirror, so its grid is only on the pupil aperture region.
- Gradient measurements are taken use  $3 \times 3$  pixels. Thus, for a  $256 \times 256$  CCD array, assuming a circular aperture with diameter equal to 128 pixels, we obtain at best gradient approximations on a  $30 \times 30$  grid.

Fig. 4.1 provides an illustration, where the small  $x$  marks denote pixels in the CCD array, and the small circles denote locations at which the gradient approximations are measured by the WFS.

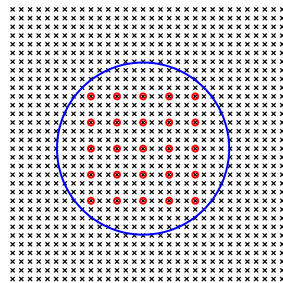


FIG. 4.1. *Example of a wavefront sensor. The large circle indicates the pupil aperture regions, the small  $x$  marks denote pixels in the CCD array, and the small circles denote locations at which the gradient approximations are measured by the WFS.*

Interpolation of the gradient data to a fine grid can be used to reconstruct the wavefront and corresponding PSFs. Although this approach may work well when the seeing conditions are good, the accuracy of the resulting wavefront and PSF may not allow for quality restorations. In the next subsection we describe an approach to obtain high resolution gradient information using multiple frames of data.

**4.2. Reconstructing High Resolution Wavefront Gradients.** A recent approach proposed by Jefferies and Hart [16] uses multiple frames of data and a *frozen flow hypothesis* (FFH) of the atmosphere to construct a composite, higher resolution grid of gradient measurements. The FFH assumes that atmospheric turbulence can be modeled by a series of independent static layers, each moving across the telescope aperture with the prevailing wind at the altitude of the layer. Because of its simplicity, the FFH is frequently used as the basis for numerical studies of telescope imaging

performance, particularly in the modeling of *adaptive optics* (AO) systems. While the FFH is observed not to hold in the real world over long time scales, a number of studies have shown that it is a reasonable approximation for short but still interesting periods [7, 19, 22].

To use the FFH to reconstruct wavefront gradients, several frames of data are collected over a short time period, each giving gradient measurements at a different set of grid points. For ease of presentation, we consider only one layer. If the motion of the atmospheric layer is known, then the measured gradient data can be combined to form a mosaic, or composite grid of measurements. This is illustrated in Fig. 4.2 with two different velocity profiles. Note that the composite grid resolution depends on the velocity profile; in the example shown in the left part of Fig. 4.2, the velocity (direction and magnitude) remains constant from frame to frame, and the magnitude of the velocity is relatively small. A more extreme situation is illustrated in the right part of Fig. 4.2, where there is a nonlinear change in the velocity from frame to frame.

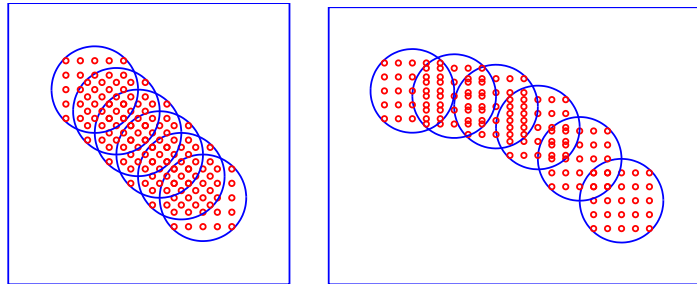


FIG. 4.2. Illustrations of building a composite, high resolution grid from six different coarse grid measurements. Each large circle represents the region in the composite image for a single frame. The small circles denote grid points at which the wavefront gradient approximations are measured. The illustration on the left depicts a situation when the velocity remains constant from frame to frame, while the illustration on the right is a situation where the velocity changes nonlinearly from frame to frame.

If the composite grid is uniform, then the high resolution wavefront gradient measurements can be obtained from the composite grid through a simple extraction process. However, a situation such as this would only occur when there is a very specific, constant velocity from frame to frame. For example, consider the simple situation illustrated in Fig. 4.3, where an underlying uniform grid is represented by  $\times$ 's, and two coarse grids are denoted by  $o$ 's. Although one frame falls directly on the underlying uniform grid, the other frame does not. Including rotation in the velocity profile will introduce additional irregularities in the composite grid of data. The computationally challenging step is to construct the composite gradient measurements on a uniform high resolution grid from the given, nonuniform, coarse grid information.

**4.3. Linear Model of Wavefront Motion.** In this subsection we describe the approach we use to model motion of the gradient fields. Suppose  $\phi_x(x, y)$  and  $\phi_y(x, y)$  are functions describing the shape of the gradient fields, and  $\Phi_x$  and  $\Phi_y$  are arrays of discrete samples of  $\phi_x(x, y)$  and  $\phi_y(x, y)$ ; that is,

$$\begin{aligned}\Phi_x(i, j) &= D_x \phi(x_i, y_j) = \phi_x(x_i, y_j), & i = 1, 2, \dots, n, & j = 1, 2, \dots, n, \\ \Phi_y(i, j) &= D_y \phi(x_i, y_j) = \phi_y(x_i, y_j), & i = 1, 2, \dots, n, & j = 1, 2, \dots, n,\end{aligned}$$

where  $D_x$  and  $D_y$  are discrete derivative operators as defined in [2]. Using the FFH, we can assume changes in the gradients, from frame to frame, are modeled as a rigid

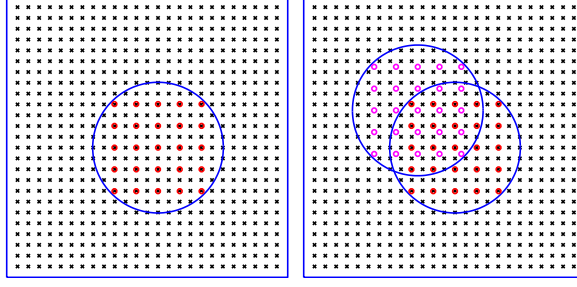


FIG. 4.3. A single frame of data can be aligned to an underlying, uniform fine grid, as illustrated with the image on the left. However, additional frames are likely to move to locations that do not fall directly on the uniform grid; this is illustrated with the image on the right. In this figure, the  $x$ 's denote points on the underlying uniform grid, and the  $o$ 's denote points on the coarse grid of each frame of WFS data.

movement of  $\phi_x(x, y)$  or  $\phi_y(x, y)$ . Rigid motion of coordinates in a plane can be described through a  $3 \times 3$  affine transformation. So if we let  $\Phi_x^{(m)}$  and  $\Phi_y^{(m)}$  be the discretization of  $\phi_x(x, y)$  and  $\phi_y(x, y)$  after a rigid movement, then

$$\begin{aligned} \Phi_x^{(m)}(i, j) &= \phi_x(\hat{x}_i, \hat{y}_j) \\ \Phi_y^{(m)}(i, j) &= \phi_y(\hat{x}_i, \hat{y}_j), \end{aligned} \quad \text{where} \quad \begin{bmatrix} \hat{x}_i \\ \hat{y}_j \\ 1 \end{bmatrix} = \begin{bmatrix} a_{11} & a_{12} & a_{13} \\ a_{21} & a_{22} & a_{23} \\ 0 & 0 & 1 \end{bmatrix} \begin{bmatrix} x_i \\ y_j \\ 1 \end{bmatrix}. \quad (4.2)$$

In practice the function  $\phi_x$  and  $\phi_y$  are not known at every point  $(x, y)$  (all that is known are the discrete values  $\Phi_x$  and  $\Phi_y$ ), so it may not be possible to evaluate  $\phi_x(\hat{x}_i, \hat{y}_j)$  or  $\phi_y(\hat{x}_i, \hat{y}_j)$ , unless  $\hat{x}_i = x_{\hat{i}}$  and  $\hat{y}_j = y_{\hat{j}}$  for integers  $\hat{i}$  and  $\hat{j}$ ,  $1 \leq \hat{i} \leq n$  and  $1 \leq \hat{j} \leq n$ . However, approximations of  $\phi_x(\hat{x}_i, \hat{y}_j)$  and  $\phi_y(\hat{x}_i, \hat{y}_j)$  can be computed by interpolating known values of  $\phi_x$  and  $\phi_y$  near  $\phi_x(\hat{x}_i, \hat{y}_j)$  and  $\phi_y(\hat{x}_i, \hat{y}_j)$ . Suppose, as illustrated in Fig. 4.4, that  $\phi_x(x_{\hat{i}}, y_{\hat{j}})$ ,  $\phi_x(x_{\hat{i}+1}, y_{\hat{j}})$ ,  $\phi_x(x_{\hat{i}}, y_{\hat{j}+1})$  and  $\phi_x(x_{\hat{i}+1}, y_{\hat{j}+1})$  are four known pixel values surrounding the unknown value  $\phi_x(\hat{x}_i, \hat{y}_j)$ . Bilinear interpolation uses a weighted average of the four pixels surrounding  $\phi_x(\hat{x}_i, \hat{y}_j)$  for the approximation. The same idea can be used to compute  $\phi_y(\hat{x}_i, \hat{y}_j)$ . Assuming, without loss of generality that the distance between pixel centers is one, then the weights for bilinear interpolation are given as

$$\begin{aligned} \Phi_x^{(m)}(i, j) &= \phi_x(\hat{x}_i, \hat{y}_j) \\ &\approx (1 - \Delta x_i)(1 - \Delta y_j)\phi_x(x_{\hat{i}}, y_{\hat{j}}) + (1 - \Delta x_i)\Delta y_j\phi_x(x_{\hat{i}}, y_{\hat{j}+1}) \\ &\quad + \Delta x_i(1 - \Delta y_j)\phi_x(x_{\hat{i}+1}, y_{\hat{j}}) + \Delta x_i\Delta y_j\phi_x(x_{\hat{i}+1}, y_{\hat{j}+1}), \end{aligned}$$

where  $\Delta x_i = \hat{x}_i - x_{\hat{i}}$  and  $\Delta y_j = \hat{y}_j - y_{\hat{j}}$ . This also holds for the  $\Phi_y^{(m)}(i, j)$ .

If we define vectors  $\phi_x = \text{vec}(\Phi_x)$ ,  $\phi_y = \text{vec}(\Phi_y)$  and  $\phi_x^{(m)} = \text{vec}(\Phi_x^{(m)})$ ,  $\phi_y^{(m)} = \text{vec}(\Phi_y^{(m)})$  from the discrete data arrays (e.g., through lexicographical ordering), we can write

$$\phi_x^{(m)} = \mathbf{A}_m \phi_x, \quad \phi_y^{(m)} = \mathbf{A}_m \phi_y,$$

where  $\mathbf{A}_m$  is a sparse matrix that contains the interpolation weights. Specifically, the  $k$ th row of  $\mathbf{A}_m$  contains the weights for the pixel in the  $k$ th entry of  $\phi_x^{(m)}$  or  $\phi_y^{(m)}$ .

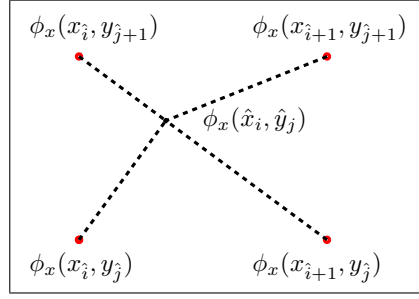


FIG. 4.4. Illustration of bilinear interpolation, where a weighted average of the four known discrete values is used to approximate  $\phi_x(\hat{x}_i, \hat{y}_j)$ .

That is, in the case of bilinear interpolation, there are at most four nonzero entries per row, given by

$$(1 - \Delta x_i)(1 - \Delta y_j), \quad (1 - \Delta x_i)\Delta y_j, \quad \Delta x_i(1 - \Delta y_j), \quad \Delta x_i\Delta y_j.$$

We emphasize that by using a sparse data format (e.g., compressed row [4]) to represent  $\mathbf{A}_m$ , we need only keep track of the nonzero entries and their locations in the matrix  $\mathbf{A}_m$ . Moreover, this discussion assumes that the affine transformation used in equation (4.2) is known from wind velocity information.

As explained in a previous subsection, we cannot measure the wavefront directly, but instead we observe gradients on a low resolution grid. The mathematical formulation of this process is given by:

$$\phi_x^{(m)} = \mathbf{R}\mathbf{W}\mathbf{A}_m\mathbf{D}_x\phi \quad \text{and} \quad \phi_y^{(m)} = \mathbf{R}\mathbf{W}\mathbf{A}_m\mathbf{D}_y\phi,$$

where  $\mathbf{W}$  is an indicator matrix that grabs a specified section of  $\phi_x$  and  $\phi_y$ , and  $\mathbf{R}$  is a sparse downsampling (or restriction) matrix that transforms high resolution data to a lower resolution. More specifically,

- $\mathbf{W}$  is a full row rank, underdetermined matrix with zeros and ones. For example, suppose

$$\Phi = \begin{bmatrix} \phi_1 & \phi_4 & \phi_7 \\ \phi_2 & \phi_5 & \phi_8 \\ \phi_3 & \phi_6 & \phi_9 \end{bmatrix}, \quad \phi = \text{vec}(\Phi)$$

and

$$\mathbf{W} = \begin{bmatrix} 0 & 0 & 0 & 1 & 0 & 0 & 0 & 0 & 0 \\ 0 & 0 & 0 & 0 & 1 & 0 & 0 & 0 & 0 \\ 0 & 0 & 0 & 0 & 0 & 0 & 1 & 0 & 0 \\ 0 & 0 & 0 & 0 & 0 & 0 & 0 & 1 & 0 \end{bmatrix}$$

then

$$\text{vec} \left( \begin{bmatrix} \phi_4 & \phi_7 \\ \phi_5 & \phi_8 \end{bmatrix} \right) = \mathbf{W}\phi.$$

- To describe  $\mathbf{R}$ , suppose  $\Phi \in \mathcal{R}^{n \times n}$  is an array of data on a high resolution,  $n \times n$ , grid, and that we want to downsample this to an  $m \times m$  grid, where  $s = n/m$  is an integer. Then

$$\mathbf{R} = (\mathbf{R}_1 \otimes \mathbf{R}_1)/(s^2)$$

where  $\mathbf{R}_1 = \mathbf{I}_m \otimes \mathbf{1}_s^T$ ,  $\mathbf{I}_m$  is an  $m \times m$  identity matrix, and  $\mathbf{1}_s$  is vector of length  $s$  containing all ones. Note that  $\mathbf{R}$  is underdetermined, but has full row rank.

Assuming that we obtain  $m$  frames of data, we have

$$\begin{bmatrix} \phi_x^{(1:m)} \\ \phi_y^{(1:m)} \end{bmatrix} = \begin{bmatrix} (\mathbf{I} \otimes \mathbf{R}\mathbf{W})\mathbf{A}\mathbf{D}_x \\ (\mathbf{I} \otimes \mathbf{R}\mathbf{W})\mathbf{A}\mathbf{D}_y \end{bmatrix} \phi$$

where  $\mathbf{R}$ ,  $\mathbf{W}$ ,  $\mathbf{D}_x$ ,  $\mathbf{D}_y$  were previously described,  $\otimes$  denotes Kronecker product,  $\mathbf{I}$  is an  $m \times m$  identity matrix, and

$$\phi_x^{(1:m)} = \begin{bmatrix} \phi_x^{(1)} \\ \phi_x^{(2)} \\ \vdots \\ \phi_x^{(m)} \end{bmatrix}, \quad \phi_y^{(1:m)} = \begin{bmatrix} \phi_y^{(1)} \\ \phi_y^{(2)} \\ \vdots \\ \phi_y^{(m)} \end{bmatrix}, \quad \mathbf{A} = \begin{bmatrix} \mathbf{A}_1 \\ \mathbf{A}_2 \\ \vdots \\ \mathbf{A}_m \end{bmatrix}.$$

In this model,  $\phi$  represents a large, global wavefront, but at the time each frame of data is collected, the telescope detects only a small subregion of information, which is modeled by the matrix  $\mathbf{W}$ .

Note that it is impossible to reconstruct the whole global wavefront  $\phi$  because we cannot collect enough gradient data to cover the whole wavefront region. However, we can construct a composite of the collected information on a high resolution grid by two steps: first, solve a underdetermined least squares problem for the composite horizontal and vertical gradient measurements:

$$\begin{bmatrix} \phi_x^{\text{composite}} \\ \phi_y^{\text{composite}} \end{bmatrix} = \arg \min_{\phi_x, \phi_y} \left\| \begin{bmatrix} \phi_x^{(1:m)} \\ \phi_y^{(1:m)} \end{bmatrix} - \begin{bmatrix} (\mathbf{I} \otimes \mathbf{R}\mathbf{W})\mathbf{A}\phi_x \\ (\mathbf{I} \otimes \mathbf{R}\mathbf{W})\mathbf{A}\phi_y \end{bmatrix} \right\|_2^2 \quad (4.3)$$

and compute gradient measurements on finer grids for each frame by

$$\begin{bmatrix} \hat{\phi}_x^{(1:m)} \\ \hat{\phi}_y^{(1:m)} \end{bmatrix} = \begin{bmatrix} (\mathbf{I} \otimes \mathbf{W})\mathbf{A}\phi_x^{\text{composite}} \\ (\mathbf{I} \otimes \mathbf{W})\mathbf{A}\phi_y^{\text{composite}} \end{bmatrix};$$

next, use the computed gradients to solve an underdetermined least squares problem for each frame

$$\phi^{(i)} = \arg \min_{\phi} \left\| \begin{bmatrix} \hat{\phi}_x^{(i)} \\ \hat{\phi}_y^{(i)} \end{bmatrix} - \begin{bmatrix} \mathbf{D}_x \\ \mathbf{D}_y \end{bmatrix} \phi \right\|_2^2, \quad i = 1, 2, \dots, m. \quad (4.4)$$

We remark that both (4.3) and (4.4) are underdetermined, and can be sensitive to noise in the measured data. We use Tikhonov regularization [11, 23] to obtain the reconstructed images.

**4.4. Multi-Layered Atmospheric Model.** The previous subsection focused on the single layer wavefront problem. Considering a more realistic model, the atmosphere above the telescope can be split into several dominant layers, which move with different velocities [8]. For the multi-layered model, we assume that the composite high resolution wavefront at the telescope is the sum of the high resolution wavefront at each altitude. Then we have

$$\phi = \sum_{j=1}^L c_j \phi_j \quad (4.5)$$

where  $L$  is the number of turbulent layers,  $\phi$  is the wavefront at the telescope,  $\phi_j$  is the wavefront of the  $j$ th layer, and  $c_j$  is a constant such that  $\sum_{j=1}^L c_j = 1$  and specifies relative dominance in the contribution of each layer to the total turbulent field. For example, if it is assumed that all layers contribute equally to the total wavefront hitting the telescope, then  $c_1 = c_2 = \dots = c_L$ . On the other hand, if it is assumed that the  $k$ th layer is the dominant layer of the atmospheric turbulence, then  $c_k \gg c_j$ ,  $j = 1, \dots, k-1, k+1, \dots, L$ .

Similar to the single layer turbulent model, in the multi-layered case, we model this problem

$$\begin{bmatrix} \phi_x^{(1:m)} \\ \phi_y^{(1:m)} \end{bmatrix} = \begin{bmatrix} (\mathbf{I} \otimes \mathbf{R}\mathbf{W})\mathbf{A}_1\mathbf{D}_x & \cdots & (\mathbf{I} \otimes \mathbf{R}\mathbf{W})\mathbf{A}_L\mathbf{D}_x \\ (\mathbf{I} \otimes \mathbf{R}\mathbf{W})\mathbf{A}_1\mathbf{D}_y & \cdots & (\mathbf{I} \otimes \mathbf{R}\mathbf{W})\mathbf{A}_L\mathbf{D}_y \end{bmatrix} \begin{bmatrix} \phi_1 \\ \vdots \\ \phi_L \end{bmatrix}$$

where  $\mathbf{R}$ ,  $\mathbf{W}$ ,  $\mathbf{D}_x$ ,  $\mathbf{D}_y$  were previously described,  $\otimes$  denotes Kronecker product,  $\mathbf{I}$  is an  $m \times m$  identity matrix,  $\phi_j$  and  $\mathbf{A}_j$ ,  $j = 1, \dots, L$ , denotes the wavefront and the matrix that defines the motion of the atmosphere for layer  $j$ , and

$$\mathbf{A}_j = \begin{bmatrix} \mathbf{A}_{1,j} \\ \mathbf{A}_{2,j} \\ \vdots \\ \mathbf{A}_{m,j} \end{bmatrix}, \quad j = 1, 2, \dots, L.$$

Note  $\mathbf{A}_{i,j}$  is the motion matrix for the  $i$ th frame of the  $j$ th layer.

We need to reconstruct the wavefront for each frame. This can be done by two steps. First, solve

$$\begin{bmatrix} \phi_{x,(1:L)}^{\text{composite}} \\ \phi_{y,(1:L)}^{\text{composite}} \end{bmatrix} = \underset{\phi_{x,(1:L)}, \phi_{y,(1:L)}}{\text{argmin}} \left\| \begin{bmatrix} \phi_x^{(1:m)} \\ \phi_y^{(1:m)} \end{bmatrix} - \begin{bmatrix} (\mathbf{I} \otimes \mathbf{R}\mathbf{W})\mathbf{A}_1\phi_{x,1} & \cdots & (\mathbf{I} \otimes \mathbf{R}\mathbf{W})\mathbf{A}_L\phi_{x,L} \\ (\mathbf{I} \otimes \mathbf{R}\mathbf{W})\mathbf{A}_1\phi_{y,1} & \cdots & (\mathbf{I} \otimes \mathbf{R}\mathbf{W})\mathbf{A}_L\phi_{y,L} \end{bmatrix} \right\| \quad (4.6)$$

and compute

$$\begin{bmatrix} \hat{\phi}_x^{(1:m)} \\ \hat{\phi}_y^{(1:m)} \end{bmatrix} = \begin{bmatrix} (\mathbf{I} \otimes \mathbf{W})\mathbf{A}_1\phi_{x,1}^{\text{composite}} & \cdots & (\mathbf{I} \otimes \mathbf{W})\mathbf{A}_L\phi_{x,L}^{\text{composite}} \\ (\mathbf{I} \otimes \mathbf{W})\mathbf{A}_1\phi_{y,1}^{\text{composite}} & \cdots & (\mathbf{I} \otimes \mathbf{W})\mathbf{A}_L\phi_{y,L}^{\text{composite}} \end{bmatrix},$$

where  $\phi_{x,j}$ ,  $\phi_{y,j}$ ,  $j = 1, \dots, L$ , are composite gradients of the  $j$ th layer,  $\phi_x^{(1:m)}$ ,  $\phi_y^{(1:m)}$ ,  $\hat{\phi}_x^{(1:m)}$ ,  $\hat{\phi}_y^{(1:m)}$ ,  $\mathbf{I}$ ,  $\mathbf{R}$  and  $\mathbf{W}$  are defined as before, and

$$\phi_{x,(1:L)} = \begin{bmatrix} \phi_{x,1} \\ \phi_{x,2} \\ \vdots \\ \phi_{x,L} \end{bmatrix}, \quad \phi_{y,(1:L)} = \begin{bmatrix} \phi_{y,1} \\ \phi_{y,2} \\ \vdots \\ \phi_{y,L} \end{bmatrix},$$

Next, solve

$$\phi^{(i)} = \underset{\phi}{\text{argmin}} \left\| \begin{bmatrix} \hat{\phi}_x^{(i)} \\ \hat{\phi}_y^{(i)} \end{bmatrix} - \begin{bmatrix} \mathbf{D}_x \\ \mathbf{D}_y \end{bmatrix} \phi \right\|_2^2, \quad i = 1, \dots, m. \quad (4.7)$$

Again, (4.6) and (4.7) are underdetermined.

**5. Numerical Experiments.** In this section we present results from some numerical experiments using a realistic model of atmospheric turbulence. Specifically, we used the approach described in [21] to generate a global wavefront phase, assuming that the diameter of the telescope is 3.7 m, the light wavelength is  $0.744 \times 10^{-6}$  m, the propagation distance is 25 km, there are three dominant layers moving in different directions, and we assume that 50 frames of data are collected. Gaussian white noise (1%) was added to the measured gradients, as well as to the blurred images. The wind speed information for each layer used in our experiments is shown in Table 5.1. We report on results using these basic parameters, modifying only the turbulence strength.

TABLE 5.1  
*Turbulent layers*

layer	location (km)	wind speed (pixel/frame)	wind direction
1	0	0.1730	horizontally
2	11	0.9686	vertically
3	15	0.5189	diagonally

There are three regularized systems to be solved for reconstructing the images: first, we need to compute gradients on a finer grid (4.6); next, we construct wavefronts for each frame (4.7); and finally, to restore the image, we compute an FFT-based WLS solution using equation (3.1). To choose weights for our experiments, since we know the true PSFs, we compute the relative errors of PSFs obtained from the reconstructed wavefront phases, and use the reciprocals of the errors as the weights. We realize that this scheme for choosing weights is not possible for a realistic problem, but a very similar approach based on the sampling of the overlapping frames could be used in practice; frames with better sampling have larger weights, while frames with poor sampling have smaller weights.

For each system, we need to assign regularization parameters, and since (4.6) and (4.7) are solved iteratively using LSQR, we need to choose a stopping tolerance for these. Specifically, in the first least squares problem we used Tikhonov regularization with a regularization parameter 1e-3 and LSQR to solve, with a stopping tolerance (relative residual) of 1e-3. In the second least squares problem, we again used 1e-3 as a regularization parameter and LSQR to solve, with a stopping tolerance (relative residual) of 1e-6. In the final multi-frame deconvolution problem, we used Tikhonov regularization and FFT-based spectral decompositions in GCV to choose the regularization parameter.

The size of the least squares system for the FFH reconstruction depends on the image size and wind velocity (which determines the size of the composite gradients), as well as the downsampling factor. In our experiments, the image size of each frame is  $256 \times 256$ , and using the wind velocity listed in Table 5.1, the grid for the composite gradients is  $304 \times 304$ . The downsampling factor is 4, resulting in a low resolution grid that is  $64 \times 64$ . Therefore, the size of the least squares problem in (4.6) is  $204,800 \times 277,248$ .

**5.1. Example: Good Seeing Conditions.** In this first test, we simulate motion of the wavefront using the velocity profile listed in Table 5.1 with  $d/r_0 = 5$ . In this case, the seeing conditions are good, and so we expect a smooth wavefront, and an observed image with very little blurring. This is illustrated in Fig. 5.1.

In order to restore the image, we need to compute the composite horizontal and

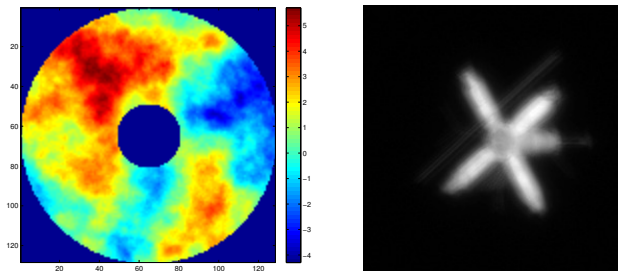


FIG. 5.1. First frame of the wavefront phase, and the corresponding observed image, for  $d/r_0 = 5$ . In this case, the seeing conditions are good, resulting in smooth wavefront phases and only slightly blurred observed images.

vertical gradient measurements on a finer grid by solving the least squares problem (4.6), and then reconstruct the approximate wavefront phase by solving the least squares problem (4.7). We also use a naïve approach, which simply interpolates the gradients to a finer grid. To obtain a quantitative measure of the effectiveness of our FFH approach, we compare the reconstructed PSFs with the true PSFs; Fig. 5.2 shows a plot of the relative errors of the reconstructed PSFs for each of the 50 frames. The FFH approach produces much better approximations of the PSFs than the naïve approach. The more accurate PSFs result in a slightly better reconstructed image, which are displayed in Fig. 5.3. Because the seeing conditions are very good in this example, the naïve approach does quite well, and there is only a slight improvement with our FFH approach.

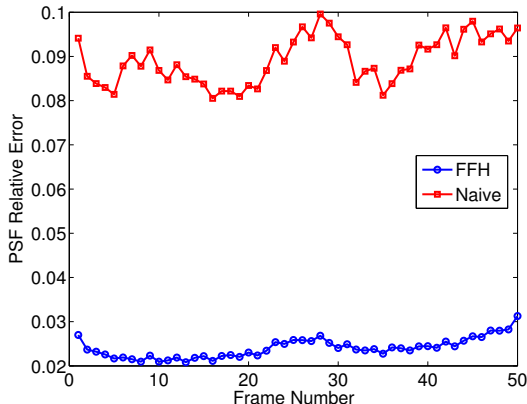


FIG. 5.2. Plot of the relative errors of the reconstructed PSF for each frame using two different approaches when  $d/r_0 = 5$ .

**5.2. Example: Poor Seeing Conditions.** In this example, we simulate motion of the wavefront for the case  $d/r_0 = 20$ . In this case, the seeing conditions are poor, and so we expect to see more severe oscillations in the wavefront, and much more blurring in the observed image as compared with the previous example. This is illustrated in Fig. 5.4.

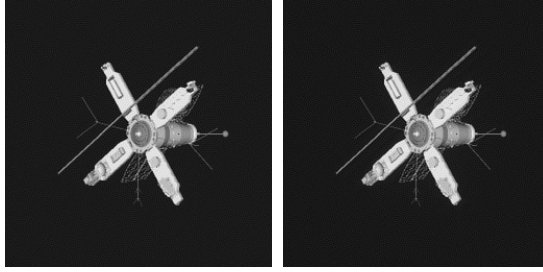


FIG. 5.3. Comparison of reconstructed images for  $d/r_0 = 5$ ; the reconstructed image by multiple layer FFH model is on the left (relative error = 0.1178), and the reconstructed image by naïve approach is on the right (relative error = 0.1336).

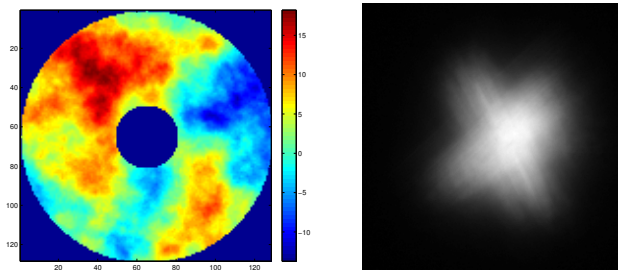


FIG. 5.4. First frame of the wavefront phase, and the corresponding observed image, for  $d/r_0 = 20$ . In this case, the seeing conditions are poor, resulting in oscillatory wavefront phases and more severely blurred observed images.

Again, we compared our FFH approach with the naïve scheme of interpolating the low resolution gradients to the higher resolution grid by investigating the quality of the reconstructed PSFs for each approach. Fig. 5.5 shows the relative errors of the reconstructed PSFs, and Fig. 5.6 displays the reconstructed images obtained by the two approaches. In this case, there is a clear advantage to using more the accurate PSFs from our FFH approach to reconstruct the image.

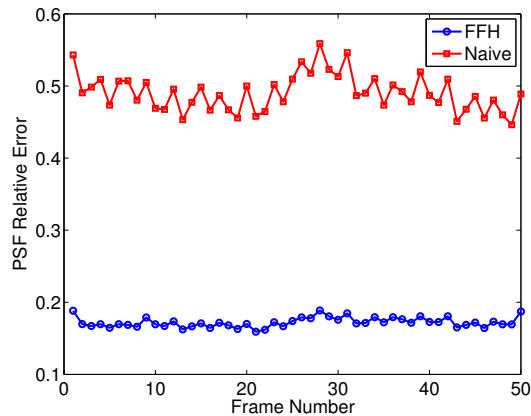


FIG. 5.5. Plot of the relative errors of the reconstructed PSF for each frame using two different approaches when  $d/r_0 = 20$ .

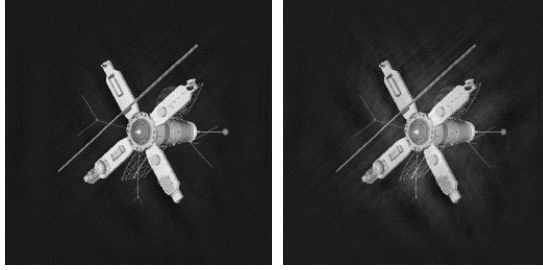


FIG. 5.6. Comparison of the reconstructed images for  $d/r_0 = 20$ ; the reconstructed image by multiple layer FFH model is on the left (relative error = 0.1709), and the reconstructed image by naïve approach is on the right (relative error = 0.3272).

**5.3. Example: Extremely Poor Seeing Conditions.** In this final example, we simulate motion of the wavefront for an extreme case  $d/r_0 = 45$ . In this case, the wavefront is highly oscillatory and the observed images are severely blurred. This is illustrated in Fig. 5.7. Fig. 5.8 shows the relative errors of the reconstructed PSFs, using our FFH approach and the naïve approach, and Fig. 5.9 shows that the reconstructed image. As can be seen from this example, it is essential to obtain accurate estimates of the PSFs when attempting to reconstruct extremely blurred images. In particular, if we attempt to use gradients measured by a telescope’s wavefront sensor to reconstruct a single image frame, the highly oscillatory nature of the wavefront does not provide enough information to expect to get an accurate estimate of the high resolution gradients (and, hence, the corresponding wavefront phase and PSF) by simply interpolating the low resolution measurements to a high resolution grid. It is essential to obtain additional information about the gradients on the high resolution grid, such as we have proposed in this paper with the FFH model of the wavefront.

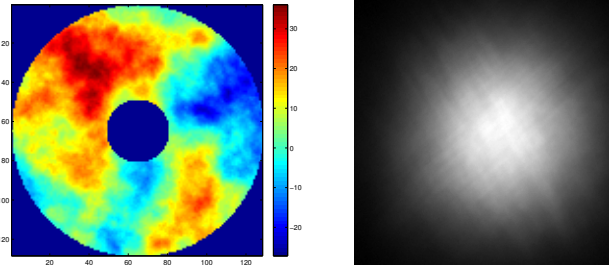


FIG. 5.7. First frame of the wavefront phase, and the corresponding observed image, for  $d/r_0 = 45$ . In this case, the seeing conditions are extremely poor, resulting in highly oscillatory wavefront phases and extremely blurred observed images.

**5.4. Remarks on Computational Cost.** The least squares problem (4.7) and the multi-frame deconvolution problem are well understood, and there are many approaches to solve these problems. The new contribution of this paper is the FFH gradient reconstruction, which requires solving the least squares problem (4.6). The structure and sparsity of this problem depends on the wind velocity. For example, if the wind velocity results in uniform shifts that are an integer multiple of the (high

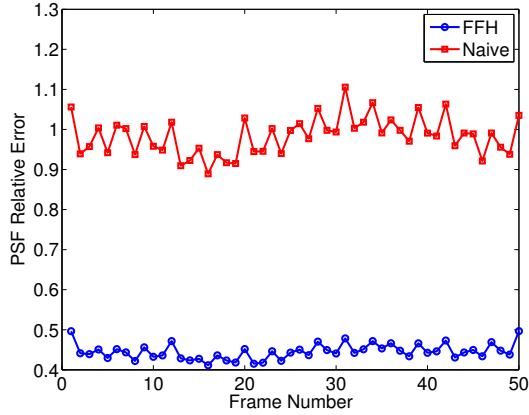


FIG. 5.8. Plot of the relative errors of the reconstructed PSF for each frame using two different approaches when  $d/r_0 = 45$ .

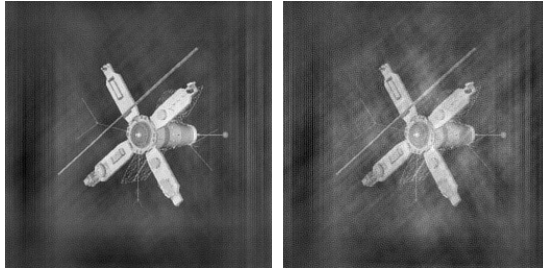


FIG. 5.9. Comparison of the reconstructed images for  $d/r_0 = 45$ ; the reconstructed image by multiple layer FFH model is on the left (relative error = 0.3777), and the reconstructed image by naïve approach is on the right (relative error = 0.6195).

resolution) pixel size, then there may be some structure (e.g., Toeplitz) that can be exploited when solving this least squares problem. However, for realistic problems, the wind velocity may result in nonuniform shifts, and the shifts are not likely to be integer multiples of the pixel size. Thus, there is no obvious general approach that exploits structure when solving this least squares problem.

However, we do exploit sparsity. In particular, in the experiments reported in this paper, the number of non-zeroes in the  $204,800 \times 277,248$  coefficient matrix in equation (4.6) is 2,616,204, or approximately 13 unknowns per row. The number of LSQR iterations needed to solve equations (4.6) and (4.7) for each of the examples discussed in this section is reported in Table 5.2.

TABLE 5.2

This table displays the number of LSQR iterations needed to compute  $x$  and  $y$ -gradients, as well as the average number of iterations needed for the wavefront reconstruction of each frame.

$\frac{d}{r_0}$	$\phi_x$	$\phi_y$	$\phi$ (FFH)	$\phi$ (naïve)
5	220	219	54	41
20	215	219	54	41
45	215	216	54	41

**6. Concluding Remarks.** In this paper we described how practical deblurring of images distorted by atmospheric turbulence requires solving three large scale least squares problems:

- Reconstructing high resolution wavefront phase gradients from low resolution measurements obtained from a wavefront sensor on the telescope.
- Reconstructing wavefront phases from wavefront phase gradients.
- Reconstructing the image using an atmospheric blurring model that depends on the wavefront phase.

The main contribution of this paper is to describe a mathematical model, based on a frozen flow hypothesis, that allows for reconstruction of more accurate high resolution gradients than existing approaches. The frozen flow hypothesis captures the inherent temporal correlations present in wavefronts in consecutive frames of data. Exploiting these correlations can lead to more accurate PSF estimations, as illustrated by the numerical experiments in this paper. We also showed that the FFH model can be formulated as a sparse least squares problem that can be efficiently solved with iterative methods such as LSQR.

There are several open issues not addressed in this paper. For example, we do not have an automatic approach for choosing regularization parameters, and in this regard, hybrid methods (see, for example, [3] and the references therein) might be useful. In addition, it might be worth investigating alternatives to Tikhonov regularization. We also mention that the frozen flow model is only valid for short time periods. For long time periods, it might be necessary to partition the frames into sub-time periods over which the frozen flow is valid. Currently we assume the wind speeds are known to high accuracy. Therefore, another issue worth investigation, if there is uncertainty in the wind speeds, is to reformulate the FFH reconstruction as a separable nonlinear least squares problem, where the wind speeds are considered as unknowns. Finally, because we obtain only an approximation of the wavefront phases, we only have an approximation of the corresponding PSFs. Further improvement of the PSFs and reconstructed image might be possible using multi-frame blind deconvolution algorithms. In this case, our approach can be used to obtain an initial guess for the PSFs.

#### REFERENCES

- [1] J. M. BARDSLEY, *Wavefront reconstruction methods for adaptive optics systems on ground-based telescopes*, SIAM J. Matrix Anal. Appl., 30 (2008), pp. 67–83.
- [2] J. M. BARDSLEY, S. KNEPPER, AND J. G. NAGY, *Structured linear algebra problems in adaptive optics imaging*, Adv. Comput. Math., 35 (2011), pp. 103–117.
- [3] J. CHUNG, J. G. NAGY, AND D. P. O’LEARY, *A weighted GCV method for Lanczos hybrid regularization*, Elec. Trans. Numer. Anal., 28 (2008), pp. 149–167.
- [4] T. A. DAVIS, *Direct Methods for Sparse Linear Systems (Fundamentals of Algorithms 2)*, SIAM, Philadelphia, PA, US, 2006.
- [5] H. W. ENGL, M. HANKE, AND A. NEUBAUER, *Regularization of inverse problems*, Kluwer Academic Publishers, Dordrecht, 2000.
- [6] D. L. FRIED, *Least-square fitting a wave-front distortion estimate to an array of phase-difference measurements*, J. Opt. Soc. Am, 67 (1977), pp. 370–375.
- [7] E. GENDRON AND P. LÉNA, *Single layer atmospheric turbulence demonstrated by adaptive optics observations, astrophysics and space science*, Astrophysics and Space Science, 239 (1996), pp. 221–228.
- [8] E. GERSHNIK AND E. N. RIBAK, *Light propagation through multilayer atmospheric turbulence*, Optics Communications, 142 (1997), pp. 99–105.
- [9] L. GILLES, *Order-N sparse minimum-variance open-loop reconstructor for extreme adaptive optics*, Optics Letters, 28 (2003), pp. 1927–1929.

- [10] G. H. GOLUB AND C. F. V. LOAN, *Matrix computations (3rd ed.)*, Johns Hopkins University Press, Baltimore, MD, US, 1996.
- [11] C. W. GROETSCH, *The Theory of Tikhonov Regularization for Fredholm Integral Equations of the First Kind*, Pitman Advanced Pub. Program, Boston, MA, US, 1984.
- [12] P. C. HANSEN, *Rank-deficient and discrete ill-posed problems: numerical aspects of linear inversion*, SIAM, Philadelphia, PA, US, 1998.
- [13] P. C. HANSEN, J. G. NAGY, AND D. P. O'LEARY, *Deblurring Images: Matrices, Spectra, and Filtering*, SIAM, Philadelphia, PA, US, 2006.
- [14] R. H. HUDGIN, *Wave-front reconstruction for compensated imaging*, J. Opt. Soc. Am, 67 (1977), pp. 375–378.
- [15] A. K. JAIN, *Fundamentals of Digital Image Processing*, Prentice-Hall, Inc., Upper Saddle River, NJ, US, 1989.
- [16] S. M. JEFFERIES AND M. HART, *Deconvolution from wave front sensing using the frozen flow hypothesis*, Opt. Express, 19 (2011), pp. 1975–1984.
- [17] H. NYQUIST, *Certain topics in telegraph transmission theory*, Trans. AIEE, 47 (1928), pp. 617–644.
- [18] L. A. POYNEER, D. T. GAVEL, AND J. M. BRASE, *Fast wave-front reconstruction in large adaptive optics systems with use of the fourier transform*, J. Opt. Soc. Am. A., 19 (2002), pp. 2100–2111.
- [19] L. A. POYNEER, M. VAN DAM, AND J. P. VÉRAN, *Experimental verification of the frozen flow atmospheric turbulence assumption with use of astronomical adaptive optics telemetry*, J. Opt. Soc. Am. A., 26 (2009), pp. 833–846.
- [20] H. REN AND R. DEKANY, *Fast wave-front reconstruction by solving the Sylvester equation with the alternating direction implicit method*, Opt. Express, 12 (2004), pp. 3279–3296.
- [21] J. D. SCHMIDT, *Numerical Simulation of Optical Wave Propagation with Examples in MATLAB*, SPIE Press, Bellingham, WA, US, 2010.
- [22] M. SCHÖCK AND E. J. SPILLAR, *Method for a quantitative investigation of the frozen flow hypothesis*, J. Opt. Soc. Am. A., 17 (2000), pp. 1650–1658.
- [23] A. N. TIKHONOV, A. V. GONCHARSKY, V. V. STEPANOV, AND A. G. YAGOLA, *Numerical Methods for the Solution of Ill-Posed Problems*, Kluwer Academic Publishers, Moscow, Russia, 1990.
- [24] C. R. VOGEL, *Computational Methods for Inverse Problems*, SIAM, Philadelphia, PA, US, 2002.